
TINYCD: A (NOT SO) DEEP LEARNING MODEL FOR CHANGE DETECTION

Andrea Codegoni

Dipartimento di Matematica "F. Casorati"

University of Pavia

andrea.codegoni01@ateneopv.it

Gabriele Lombardi, Alessandro Ferrari

ARGO Vision

Milano

{gabriele.lombardi,alessandro.ferrari}@argo.vision

ABSTRACT

In this paper, we present a lightweight and effective change detection model, called TinyCD. This model has been designed to be faster and smaller than current state-of-the-art change detection models due to industrial needs. Despite being from 13 to 140 times smaller than the compared change detection models, and exposing at least a quarter of the computational complexity, our model outperforms the current state-of-the-art models by at least 1% on both F1 score and IoU on the LEVIR-CD dataset, and more than 8% on the WHU-CD dataset. To reach these results, TinyCD uses a Siamese U-Net architecture exploiting low-level features in a globally temporal and locally spatial way. In addition, it adopts a new strategy to mix features in the space-time domain both to merge the embeddings obtained from the Siamese backbones, and, coupled with an MLP block, it forms a novel space-semantic attention mechanism, the Mix and Attention Mask Block (MAMB). Source code, models and results are available here: https://github.com/AndreaCodegoni/Tiny_model_4_CD

Keywords Change Detection (CD) · Remote Sensing (RS) · Convolutional Neural Network (CNN)

1 Introduction

In the Remote Sensing community, Change Detection (from now denoted with CD) is one of the main research topics. The main purpose of CD is to identify changes occurred in a scene between two different times. To this aim, a CD model compares two co-registered images I_1 and I_2 acquired at times t_1 and t_2 [1–3]. Once the relevant changes have been identified, such as urban expansion, deforestation, or post disaster damage assessment [4–10], the challenge is to let the CD model ignore other irrelevant changes. Examples of irrelevant changes are, but not limited to, lighting conditions, shadows, and seasonal variations.

Thanks to the increasing number of available high resolution aerial images datasets, such as [4, 8, 9], data driven methods like deep Convolutional Neural Networks (CNN) found successful applicability [11]. The well known ability of deep CNNs to extract complex and relevant features from images is the key factor for their early promising results [12]. In the CD scenario, complex features are important, but are not sufficient to accomplish the task. To detect the occurred changes, it is in fact crucial to model the spatio-temporal dependencies between the two images. Unfortunately, plain CNNs have a limited receptive field due to the usage of fixed kernels in convolutions. To overcome this issue, recent works focused their attention to enlarging the receptive fields by employing different kernel types [13], or by adding attention mechanisms [4, 8, 14, 15, 15–17]. However, most of them failed to explicitly relate data in the temporal domain, since attention mechanisms are applied separately on the two images. The self attention mechanism adopted in [4, 17] shows promising results relating images in the spatio-temporal domain. More recently, Transformers have been introduced in CD because of their receptive fields spatially covering the whole image [18, 19]. Notice that, by applying multi-headed attention layers in the decoder part of the network, the receptive field covers the temporal domain too. Unfortunately, the resulting models are computationally very inefficient.

The CD field finds applicability also outside the remote sensing world. As an example, in [10, 20] two models are discussed in order to be used on drones or other autonomous vehicles to implement smart city monitoring functions. In our case, the change detection model has been developed for an industrial application. In our application field, the need for real-time performances adds a model complexity constraint. Unfortunately, the majority of state-of-the-art (SOTA) models are millions-parameters-sized, so that their applicability is not possible. Another issue with those big models is related to the training time clearly affected by the size of the model. With large models, the Hyper-Parameters-Optimization (HPO) task requires resources that are usually not available to medium-small companies. Moreover, big networks require dedicated hardware also at inference time. This is in contrast with production requirements and project budgets. The search for models having both small size and performances comparable to the current SOTA can be considered an open problem.

A possible strategy to cope with both model size and complexity that, to the best of our knowledge, has not been studied in the literature, is to use low-level features to compare the two images under examination. Another underestimated aspect, in our opinion, is that a Siamese type backbone produces two tensors containing channels arranged semantically in the same order. This observation could be used to design strategies for merging features more efficiently.

The main purpose of our work is to investigate the aforementioned issues developing a neural network that requires lower computational complexity with respect to the SOTA CD models reaching at the same time comparable performances.

The major contributions of our work are the following:

- We explore the effectiveness of using low-level features in the problem of comparing images. The results validate our intuition that in this context the low-level features are sufficiently expressive. Moreover, this allowed us to significantly limit the number of model parameters.
- We introduce a novel strategy to mix the features between the two images. This strategy allows the computation of a spatio-temporal correlation between the input images keeping a low computational complexity.
- A fast attention mechanism is introduced with a block called MAMB. It uses features localized in space to compute attention masks needed in the up-sampling phase to refine the low-resolution results.
- We propose to use a pixel-wise classifier to generate the final mask. In our tests, this proved to be very effective.

Our architecture exploits the information contained in the channels of the feature vectors generated by the backbone. For this reason, it can effectively exploit low level features such that a relatively small backbone can be adopted. Being the backbone¹ the most time-consuming and parameter-demanding component in the architecture, maintaining it as small as possible allows us to achieve our goal. In particular, this allows us to maintain the total number of parameters below 300000.

Finally, we compare the quality of the model with SOTA architectures, and we demonstrate that it has performances comparable if not even superior to other SOTA models in the CD field. We have extensively tested our model on public and proprietary datasets. In order to validate and make reproducible our results, in this paper we highlight the results obtained in the field of aerial images on public datasets. Similar results in terms of efficiency and effectiveness have been found in non-public datasets, in application fields other than the one faced in this paper.

The paper is organized as follows. In Chapter 2 we present some related works. In Chapter 3 we describe our proposed model. In Chapter 4 we report both the results of our model on two publicly available datasets and the ablation study. Finally, in Chapter 6 we highlight some future research directions.

2 Related works

2.1 Early deep neural network works on CD

Deep learning models, and in particular CNNs, have been applied with great success in image comparison tasks [21–23], in pixel-level image classification [24–26], and they represent the SOTA in many other Computer Vision fields [27].

Models in the context of the CD must manage two inputs: one image I_1 acquired at time t_1 , and another one I_2 acquired at time t_2 . The correct use of these two inputs, and the features extracted from them, are extremely important for the well behavior of the CD model. One of the first works using deep learning techniques to the field of CD is [28]. This work highlights how deep neural networks, in particular Deep Belief Networks obtained by stratifying Restricted Boltzmann machines, are a very valid tool to compare and highlight the changes between the two images under examination. To

¹Notice that the backbone is evaluated twice in Siamese architectures.

the best of our knowledge, the first work that applies CNNs to the CD problem is [12]. In this work the authors propose two different approaches. In the first case they use a U-Net [25] type network with the Early Fusion Strategy (FC-EF), i.e. they concatenate the images I_1 and I_2 , and then they feed the U-Net with the resulting tensor. In the second case they investigate the Feature Fusion Strategy. To this aim, they employ a Siamese U-Net type network [22, 26, 29] where the two images are processed separately, and subsequently the features are fused in two different ways: concatenation (FC-Siam-conc) and subtraction (FC-Siam-diff). These fused features are then used as skip connections in the decoder. After this seminal work, an entire research line investigated both the Early Fusion Strategy [5, 15, 30, 31], and the Feature Fusion Strategy [4, 8, 13, 14, 16, 17, 32–37].

To take full advantage of the large amount of spatial information, deeper CNNs such as ResNet [38] or VGG16 [39] have been used [4, 8, 13, 17] in order to extract spatial information and group them in a hierarchical way. Unfortunately, standard convolution has a fixed receptive field that limits the capacity of modelling the context of the image. To face this issue, atrous convolutions [40] have been experimented [13]: they are able to enlarge the receptive field of convolutional kernels without increasing the number of parameters.

2.2 Attention based CNN

To definitively overcome the problem of fixed receptive field, attention mechanisms, in the forms of spatial attention [8, 14, 15], channel wise attention [8, 14–16], and also self-attention [4, 17], have been introduced. In [8], the attention mechanisms are used in the decoder part: the channel wise attention is used to re-weight each pixel after the fusion with the skip connections, while the spatial attention is adopted to spatially re-weight the pixels containing misleading information due to the up sampling step. To further exploit the interconnection between spatial and channel information, in [14] a dual attention module has been introduced. The co-attention module introduced in [16] tries to leverage correlation between features extracted from both images. Also in [16] a co-layer aggregation and a pyramid structure is used to make full use of the features extracted at each level and with different receptive fields. In [4], the non-local self attention introduced in [41], have been applied to CD. This mechanism consists in stacking the features extracted from a Siamese backbone to then apply both a basic spatial attention mechanism, and a pyramidal attention mechanism. Since these two attention blocks are applied to stacked features obtained from I_1 and I_2 , these are correlated in a non-local spatio-temporal way. Another interesting approach is the one presented in [42]. In this paper, the authors decided to combine CNNs with Object Image Analysis (OBIA) to mitigate the limited receptive field problem. In a first preprocessing phase, they segment the image and extract the patches containing objects to be compared. Subsequently, the extracted patches are compared using a CNN which then works on small patches containing more specific and detailed information.

In [20], the authors propose a temporal attention mechanism. They exploit the features extracted from I_2 to generate a query matrix which is then compared with the features extracted from I_1 . This mechanism is made dynamic by reducing the receptive field as tensors’ spatial dimension diminishes. Finally, the authors also use attention mechanisms capable of emphasizing some horizontal and vertical dependencies of recurring objects in their scenario.

2.3 Transformers in CD

Finally, the global attention mechanisms introduced with Transformers [43, 44] have also been applied to the CD problem. In [18] the authors employ a modified ResNet18 as Siamese backbone to extract features. Then, to better justify the use of Transformer blocks, they follow a parallelism between the natural language processing field, and the image processing one, by introducing the semantic tokens. Roughly speaking, semantic tokens are the pixels of the last feature tensor extracted by the backbone. The authors use this concept to illustrate that concatenating single pixels and then processing them with a transformer encoder-decoder, a pair of features tensors can be obtained that incorporates both global spatial information, and global temporal information. On the other side, in [19] the authors replace the CNN backbone with a transformer in order to exploit the global information contained in the images right from the start. In this model, the temporal aggregation is done only in the final multilayer perceptron decoder.

2.4 Relations between our work and existing models

Our work is inspired by [18]. As reported in Section 2.3, in that work the authors introduce the concept of semantic tokens, which are basically single pixels of the tensor obtained by the backbone. Then, they use a transformer in order to process these tokens and extract global spatio-temporal information. In agreement with [18], we believe that the information contained in the pixel/semantic token is crucial to obtain a good result. However, we prefer to apply channel-wise local feature comparison, limiting the semantic complexity and aggregation of adopted features to the first few backbone layers; whilst in [18] the comparison is global, being it obtained by means of transformers. Moreover, we adopt Multi Layer Perceptrons (MLPs) to compute both the spatial attention maps and the final mask, actually

facing the problem as a pixel-wise classification one. Recently, MLP blocks have received great attention in computer vision [45–51]. These architectures divide the images into patches and then process the patches with MLP blocks. Different structures of MLP blocks have been proposed to incorporate as much spatial information as possible. For example, in [46, 51] a spatial shift operator is applied in order to obtain information from different axial directions. The CycleMLP block proposed in [45] follows a similar idea but instead of applying the spatial shift operator to the features’ tensor, it composes several MLP steps capable of mimic the shift. A more refined version of these concepts is proposed in [47] where the authors employ a block which dynamically learns the spatial offset used in CycleMLP. In our model, the MLP blocks work exclusively along the channel dimension to both compute the spatio-temporal attention maps, and produce the final pixel-wise classification.

3 Proposed model

In this section we describe and motivate the structure of our model. We use a model resembling a Siamese U-Net consisting of 4 main components:

- Siamese encoders constituted by a pre-trained backbone (see Section 3.2).
- Mix and Attention Mask Block (MAMB) and bottleneck mixing block to compose backbone results (see Section 3.3).
- Up-sample decoder to refine low resolution results incorporating higher resolution data from the skip connections (see Section 3.4).
- Pixel level classifier (see Section 3.5)

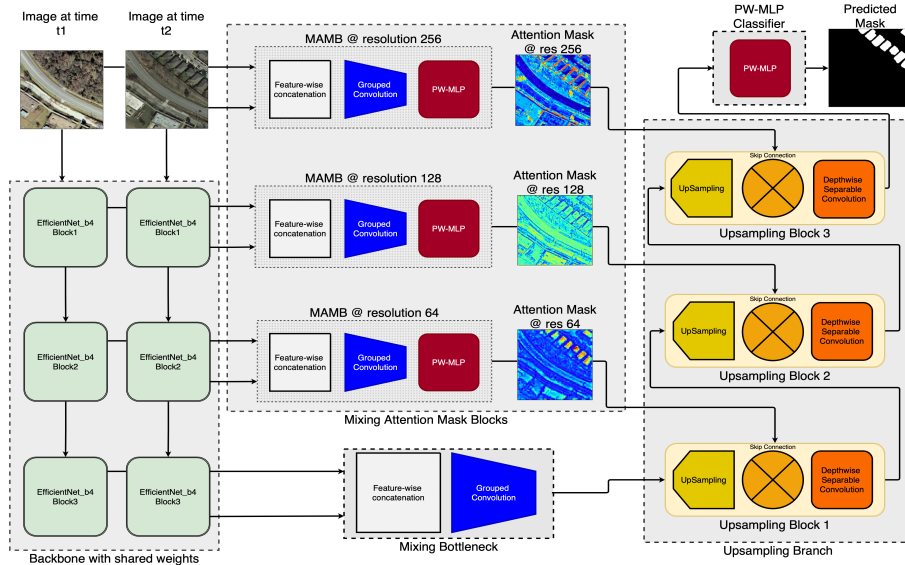


Figure 1: Siamese U-Net architecture including MAMB.

In what follows, we denote with $X \in \mathbb{R}^{(C \times H \times W)}$ the *reference* tensor (image at time t_1) and with $Y \in \mathbb{R}^{(C \times H \times W)}$ the *comparison* tensor (image at time t_2). C is the number of channels, H is the height and W the width of the tensors. We omit the batch dimension for the ease of notation. We denote with Conv the convolution operator, with PReLU the Parametric Rectified Linear Unit [52], with IN2d the Instance Normalization [53], and Sigmoid.

3.1 Model overview

Indicating with f_k the composition of the backbone blocks up to the k^{th} one, the high-level features $X_k = f_k(X)$ and $Y_k = f_k(Y)$ are extracted from each level k of the backbone. These features are used both to compute the resulting output at each level of the U-Net encoder, and to estimate the attention masks. The last backbone block produces the embeddings X_e and Y_e representing the bottleneck inputs.

Every backbone intermediate output pair (X_k, Y_k) is processed by means of the MAMB, producing spatial attention masks M_k . These masks are used as skip-connections and composed in the decoder. The last mixed tensor is obtained by composing (X_e, Y_e) .

The decoder consists of a series of up-layers, one for each block of the backbone. Each up-layer increases the spatial dimensions of the tensor received from the previous layer to reach the same resolution of the corresponding skip-connection. Furthermore, the up sampled tensors and the skip-connections are composed to generate the next layer inputs. This composition is the attention mask application to the features obtained from the previous layer.

Finally, the last block of our model classifies each pixel of the obtained tensor through a Pixel-Wise Multi-Layer Perceptron (PW-MLP). The PW-MLP associates to each pixel the probability that it belongs to the anomaly class. Applying a threshold to this tensor we obtain the binary mask of changes.

In the following subsections we describe each component separately.

3.2 Siamese encoders with pre-trained backbone

The purpose of the Siamese encoder is to extract simultaneously features from both images in a semantic coherent way. In deep neural networks, training the first layers of the model is sometimes difficult due to the well-known phenomenon of vanishing gradients [54, 55]. To overcome this problem, several tricks have been introduced such as the residual connections of ResNet [38], or the skip connections of the U-Net [25]. However, training deep backbones remains a difficult, time-consuming, or even impossible task to accomplish if the dataset is too small.

For these reasons, pre-trained backbones are often preferred, even in CD problems [4, 8, 13, 17, 18]. The disadvantage of this approach is that the backbones are not always trained on images that are similar to the ones we are dealing with. However, CNN backbones work by layering information. Low-level features, such as lines, black/white spots, points, edges, can be considered general-purpose being common to all images.

In our intuition, in the faced task the comparison between two images I_1 and I_2 , can be accomplished by using just the low-level features extracted from the first few layers of a pre-trained backbone.

We therefore decided to use one EfficientNet backbone [56] pre-trained on the ImageNet dataset [57]. We allowed the training phase to tune also the totality of the backbone parameters. Guided by experiments on our industrial dataset, the EfficientNet backbone family have been selected due to both its efficacy and its efficiency. Moreover, the resolution reduction in the first EfficientNet layers is sufficiently slow in order to create skip connections of different spatial dimensions.

For completeness, in Appendix A we compare the performance of other backbones in order to show the generality of our approach.

3.3 Mix and Attention Mask Block (MAMB) and bottleneck mixing block

The purpose of this block is to merge the features (X_k, Y_k) extracted from one of the blocks of the Siamese encoder. It creates a mask M_k that is then used as skip connection to refine the information obtained during the up-sampling phase.

The mask we create can also be understood as a pixel-level attention mechanism. The idea of pixel-wise attention has been already studied in [58]. Here we specifically designed a pixel-wise attention mechanism exploiting both spatial and temporal information.

The MAMB can be divided into two sub-blocks: the Mixing block (see Section 3.3.1), and the Pixel level mask generator (see Section 3.3.2).

3.3.1 Mixing block

As the name suggests, in this sub-block we compose the features generated by the k^{th} backbone blocks (X_k, Y_k) . To this aim, we observe that the features X_k and Y_k , share both the same shape C_k, H_k, W_k , and the same arrangement in terms of features. This means that the features in channel c of X_k have the same semantic meaning with respect to the corresponding features in channel c of Y_k , being the Siamese encoder weights shared. In view of this observation, we decided to concatenate the tensors X_k and Y_k in the tensor $Z_k \in \mathbb{R}^{2C_k \times H_k \times W_k}$ using the following rule:

$$Z_k^c := \begin{cases} X_k^{c/2} & c \text{ even} \\ Y_k^{(c-1)/2} & c \text{ odd} \end{cases} \quad \forall c \in \{0, \dots, 2C_k - 1\}. \quad (1)$$

To mix the features coming from X_k and Y_k both spatially and temporally, we used a group convolution. By choosing the number of groups equal to C_k we obtain C_k kernels of depth 2 which process the tensor Z_k in pairs of channels. These kernels perform at the same time both spatial and temporal convolution using the cross-correlation between semantically similar features.

The new tensor $Z'_k \in \mathbb{R}^{C_k \times H_k \times W_k}$ is defined as:

$$Z'_k = \text{Mix}(X_k, Y_k) := \text{PReLU}[\text{IN2d}[\text{Conv}(Z_k, ch_{in} = 2C_k, ch_{out} = C_k, groups = C_k)]]]. \quad (2)$$

An illustration of our concatenation strategy, and the following grouped convolution, is reported in Figure 2.

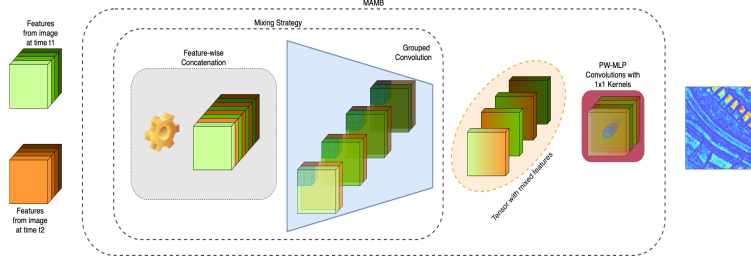


Figure 2: Visual representation of our mixing strategy and the full MAMB block. In the inner dashed block we highlight the concatenation strategy, (1), the grouped convolution, (2). These two blocks when coupled with the PW-MLP form the MAMB block.

3.3.2 Pixel-level mask generator

Fixing the spatial coordinates of a single pixel, the C_k values in the tensor Z'_k contain spatial information related to both times t_1 and t_2 . Our idea is to use the PW-MLP in order to process this information and generate a score that acts as a spatio-temporal attention.

To this aim, the PW-MLP is designed to produce a mask tensor $M_k \in \mathbb{R}^{H \times W}$.

3.3.3 PW-MLP

To implement a pixel-wise Multi-Layer Perceptron, that is an MLP working on all the channels of one single pixel at a time, we use 1×1 convolutions. The MLP is composed by N blocks each containing one 1×1 convolution and one activation function. As activation, we used the PReLU, being this able to propagate gradients also on the negative side of the real axis. The last convolution contains just one filter, thus producing a tensor M_k with dimensions 1, H_k , W_k .

The use of 1×1 convolutions to implement an MLP is not a new idea. In [59] this strategy has been used to substitute layers such as convolutions with small, trainable, networks. As pointed out in [59], we have very poor prior information on the latent concepts in pixel vectors. Hence, we have decided to use this universal function approximator to separate different semantic concepts.

3.3.4 The bottleneck mixing block

We applied the tensor mixing strategy reported in Section 3.3.1 to compute the bottleneck of the U-Net like network. More precisely, we compute: $U_e = \text{Mix}(X_e, Y_e)$.

U_e represents the output of the encoder and the input to be processed by the decoder. U_e contains the spatially and temporally correlated higher level features computed by the backbone. Given that, our intuition is that U_e contains enough information in order to classify each pixel at the bottleneck resolution.

3.4 Up-sampling decoder with skip connections

The general k -th decoder block takes as input the tensor U_{k+1} of shape $C_{k+1}, H_{k+1}, W_{k+1}$ and a mask M_k of shape $1, H_k, W_k$. Firstly, an up sampling operation is performed in order to transform U_{k+1} so that its shape matches the one of M_k . We call the up sampled tensor U'_k . Then, we define U_k with

$$U_k := \text{PReLU}[\text{IN2d}[\text{Conv}(U'_k \odot M_k)]] ,$$

where we have denoted with the symbol \odot the Hadamard product. This represents the skip connection attention mechanism at the pixel level.

As we already mentioned in Section 3.3.4, U_e contains enough information to classify each pixel at its spatial resolution. By multiplying the mask M_k , we are re-weighting each pixel in order to alleviate the misleading information generated by up sampling.

Notice that, in this Up block we employ the depth wise separable convolution [60, 61].

3.5 Pixel level classifier

Finally, since the change detection problem is a binary classification problem, we decided to use as last layer a PW-MLP with output classes $\{0, 1\}$ representing respectively normal and changed pixels. With respect to what reported in Section 3.3.3, in this case we used as the last activation layer a Sigmoid function instead of the PReLU, thus enforcing the result of the network to contain values in $[0, 1]$. In this case, the PW-MLP is used as a non-linear classifier which separates pixels in normal or changed class.

4 Experiment Settings and Results

In this section we presents the settings used in our experiments, the achieved results, and the performed ablation study.

4.1 Datasets

As already stated in Section 1, we cannot share the dataset related to our industrial application. Moreover, in order to fairly evaluate our model, and to compare it with other works in the CD field, we used the following public and widely adopted aerial building images datasets: LEVIR-CD [4] and WHU-CD [9]². Notice that the task defined by these datasets is particularly close to the faced industrial one, that is the driver of our research work. In these two datasets the model has to track some specific patters, those corresponding to buildings, and carefully segments the eventually occurred changes.

LEVIR-CD contains 637 pairs of high resolution aerial images. Starting from these images, patch pairs of size 256×256 each have been extracted. After that, the pair instances have been partitioned accordingly to the authors' original indications. This step produced 7120, 1024, and 2048 pair instances for the train, validation, and test dataset respectively.

WHU-CD contains just one pair of images having resolution 32507×15354 as a crop of a wider geographic area³. Following [62], the images have been split in non overlapping patches with resolution 256×256 . After that, a randomly partitioning of the dataset have been performed obtaining 5947, 743, and 744 pairs for train, validation, and test respectively.

4.2 Loss function and evaluation metrics

As stated in Section 3.5, we cast the CD problem in a pixel-wise binary classification setting. In fact, the role of the final MLP block is to output the per-pixel change probability.

Since the reference mask is a binary mask (0 for unchanged pixels, 1 for changed pixels), and since we are comparing probabilities, one loss function that can be used is the Binary Cross Entropy (BCE). It is defined as:

$$\mathcal{L}(G, P) := -\frac{1}{|H| \cdot |W|} \sum_{h \in H, w \in W} g_{h,w} \log(p_{h,w}) + (1 - g_{h,w}) \log(1 - p_{h,w}),$$

where we denoted with G the ground truth mask, with P the model prediction, and with H and W the set of indices relative to height and width.

Notice that the BCE loss function is widely used in other SOTA models such as [18, 19]. In contrast, other researchers implemented more sophisticated loss functions like the one presented in [4]. We decided to use the simpler BCE

²Both the adopted datasets have been obtained from <https://github.com/wgcbn/SemiCD> in an already pre-processed version.

³The whole dataset depicts the city of Christchurch, in New Zealand. The crop, aimed to be used in CD tasks, is a sub-area acquired in two different times.

in order to attribute the improvement in performances to the model and not to an ad hoc built-in loss function. For completeness, in appendix B we report other experiments conducted using other widely adopted loss functions.

To evaluate the performances achieved by our model, we calculated the *Precision (PR)*, *Recall (RC)*, *F1 score (F1)*, *Intersection over Union (IoU)* and *Overall Accuracy (OA)* with respect to the change class, as defined below:

$$\begin{aligned} Pr &:= \frac{TP}{TP + FP}, \\ Rc &:= \frac{TP}{TP + FN}, \\ F1 &:= \frac{1}{Pr^{-1} + Rc^{-1}}, \\ IoU &:= \frac{TP}{FN + FP + TP}, \\ OA &:= \frac{TP + TN}{FN + FP + TP + TN}, \end{aligned}$$

where TP, TN, FP, FN are computed on the change class, and represent the true positives, true negatives, false positives, and false negatives respectively. To retrieve the change mask we applied a 0.5 threshold to the output mask.

4.3 Implementation details

We implemented our model using PyTorch [63] and we trained it on an NVIDIA GeForce RTX 2060 6GB GPU. As described in Section 3.2, we selected the first four blocks of the EfficientNet version *b4* backbone pretrained on the ImageNet dataset. All other weights of the model have been initialized randomly⁴.

As optimizer, we adopted AdamW [64]. To optimize its hyperparameters, i.e. learning rate, weight decay and *amsgrad* variant, and also to verify the robustness of our model with respect to the choice of these parameters, we firstly run a Hyper-Parameters Optimization (HPO) task for each dataset using the package Neural Network Intelligence (NNI) [65]. After this, we fixed the learning rate equal to $3 \cdot 10^{-3}$, and the weight decay equal to $9 \cdot 10^{-3}$, for the LEVIR-CD dataset. Moreover, we fixed the learning rate equal to $2 \cdot 10^{-3}$, and the weight decay equal to $8 \cdot 10^{-3}$, for the WHU-CD dataset. For both datasets, *amsgrad* have been set to *False*. An example of the HPO procedure is reported in Appendix B. Due to computational resource limitations, no other hyperparameters have been tuned. We have not experimented network architecture search techniques (NAS).

To dynamically adjust the learning rate during the training, we adopted the cosine annealing strategy as described in [66], but avoiding the warm restart.

Since aerial images are spatially registered, we applied the geometric data augmentation operators simultaneously to the reference/comparison images and their associated ground-truth mask. Also, non-geometric augmentations are applied independently on the reference and the comparison images.

The applied geometric augmentations are Random Flip on both X and Y axes, and Random Rotation with free degree. Moreover, the applied non-geometric augmentations are Gaussian Blur and Random Brightness/Contrast change. To achieve all the adopted augmentations, we used the Albumentations library [67].

Finally, due to the limited GPU memory capacity and computational power, we fixed the batch size to 8, and trained for just 100 epochs.

4.4 Comparison with SOTA models

To demonstrate the effectiveness of our approach, we compared our results with those reported in [18, 19]. As baseline, we used the three models presented in [12]. Moreover, to compare our model with other works adopting both spatial and channel attention mechanisms, we dealt with [4, 8, 14, 36]. Finally, given the success achieved by Transformers applied to the computer vision field, we also compared our results with those obtained in [18, 19].

The results reported in Table 1 and Table 2 show the superior performance of our model on the LEVIR-CD and WHU-CD building change detection datasets.

The baseline models FC-Siam-diff and FC-Siam-conc [12] are the architectures most similar to ours. With respect to these two baseline models, we increased the F1 score by 4.73 points on LEVIR-CD, and by more than 20 points on the

⁴To make our results reproducible, we fixed the random seed at the beginning of each experiment.

Table 1: Performance metrics on the LEVIR-CD dataset. To improve results readability, we adopted a color ranking convention to represent the **First**, **Second**, and **Third** results respectively. The metrics are reported in percentage.

LEVIR-CD					
Model	Pr	Rc	F1	IoU	OA
FC-EF [12]	86.91	80.17	83.40	71.53	98.39
FC-Siam-diff [12]	89.53	83.31	86.31	75.92	98.67
FC-Siam-conc [12]	91.99	76.77	83.69	71.96	98.49
DTCDSN [14]	88.53	86.83	87.67	78.05	98.77
STANet [4]	83.81	91.00	87.26	77.40	98.66
IFNet [8]	94.02	82.93	88.13	78.77	98.87
SNUNet [36]	89.18	87.17	88.16	78.83	98.82
BIT [18]	89.24	89.37	89.31	80.68	98.92
Changeformer [19]	92.05	88.80	90.40	82.48	99.04
Ours	92.68	89.47	91.05	83.57	99.10

Table 2: Performance metrics on the WHU-CD dataset. To improve results readability, we adopted a color ranking convention to represent the **First**, **Second**, and **Third** results respectively. The metrics are reported in percentage.

WHU-CD					
Model	Pr	Rc	F1	IoU	OA
FC-EF [12]	71.63	67.25	69.37	53.11	97.61
FC-Siam-diff [12]	47.33	77.66	58.81	41.66	95.63
FC-Siam-conc [12]	60.88	73.58	66.63	49.95	97.04
DTCDSN [14]	63.92	82.30	71.95	56.19	97.42
STANet [4]	79.37	85.50	82.32	69.95	98.52
IFNet [8]	96.91	73.19	83.40	71.52	98.83
SNUNet [36]	85.60	81.49	83.50	71.67	98.71
BIT [18]	86.64	81.48	83.98	72.39	98.75
Ours	91.72	91.76	91.74	84.74	99.34

WHU-CD. With respect to the best model we found in the literature [19], our performance increment on the LEVIR-CD dataset is more limited. However, as we can see from Table 3, our model is 146.50 times smaller.

In view of these results, we can conclude that our model, despite the lower complexity and the lower number of employed parameters, is very effective on the buildings CD task. Moreover, having not used any global attention mechanism, we have a confirmation of our intuitions: in the faced CD task, low level information is sufficient to reach high-quality results. Also, the information contained in each single pixel at different resolutions, is very rich and can be exploited to effectively classify changes.

In Figure 3 a visual/qualitative comparison between the masks created by our model, and those created by BIT [18] on the LEVIR-CD test dataset, is reported. Generally speaking, both models perform well and we end up our analysis by conjecturing that the performance difference reported in Table 1 and Table 2 are more related to missing or hallucinated change regions, than region quality issues. Nevertheless, we can find some examples where there are significant differences between the ground truth masks (GT) and those created by the two models. In Figure 3 it is interesting to note that there are examples where both models fail similarly in the same regions, despite the two models being based on very different approaches (local versus global).

Table 3: Parameters, complexity, and performance comparison. The metrics are reported in percentage, parameters in Millions (M), and complexity in GFLOPs (G).

Model	Param (M)	Param ratio	FLOPs (G)	LEVIR-CD F1	WHU-CD F1
DTCDSCN [14]	41.07	146.67	7.21	87.67	71.95
STANet [4]	16.93	60.46	6.58	87.26	82.32
IFNet [8]	50.71	181.10	41.18	88.13	83.40
SNUNet [36]	12.03	42.96	27.44	88.16	83.50
BIT [18]	3.55	12.67	4.35	89.31	83.98
Changeformer [19]	41.02	146.50	N.D.	90.40	N.D.
Ours	0.28	1	1.45	91.05	91.74

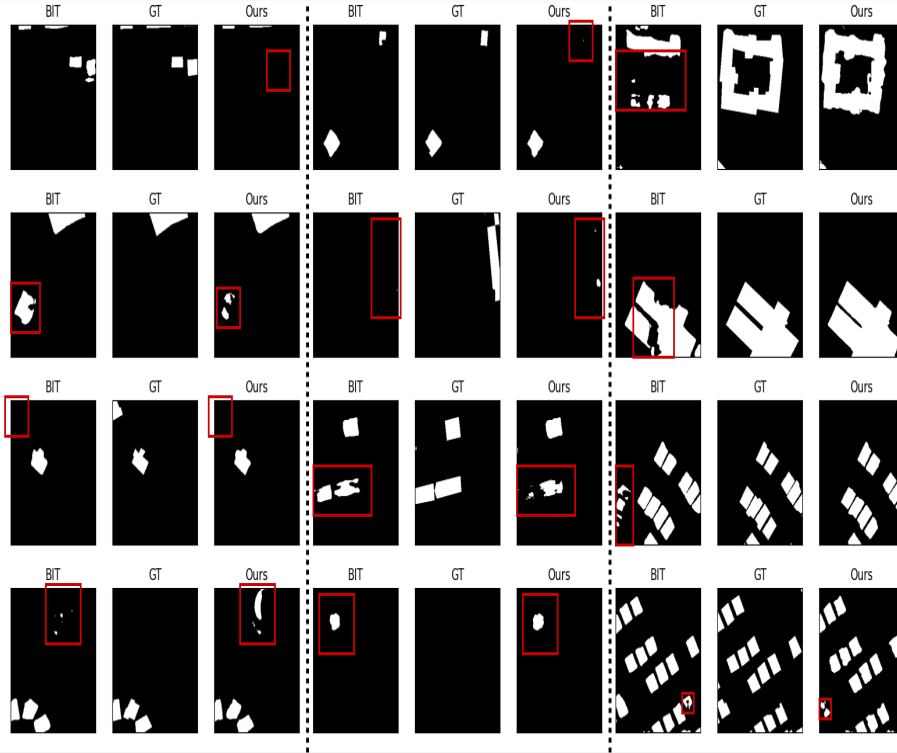


Figure 3: Visual comparison between outputs obtained by our model and BIT. We highlighted with red bounding boxes those regions containing significant differences between the ground-truth and the generated masks.

4.5 Ablation study

In this section we describe the adopted ablation study steps and the achieved results.

4.5.1 Backbone dimension and final PW-MLP

The first ablation study we conducted concerns the size of the backbone and the use of the final MLP. Regarding the backbone size, we considered both the whole EfficientNet-b4 except the final classifier, and a sliced version of the EfficientNet-b4 network including just the first 3 blocks. Moreover, to assess the effectiveness of the final classification PW-MLP block, we considered both the architecture including it, and the one that produces its output directly from the last up-sampling block by forcing its output just one channel⁵. The results shown in Table 4 confirm our intuition on

⁵We employed the sigmoid activation on this output.

low-level features. In fact, our solution with the sliced backbone and final PW-MLP, turns out to be the one with the best performances on both datasets. Furthermore, we note that, to get the best performances, the backbone slicing and PW-MLP classifier must be coupled. In fact, on LEVIR-CD the backbone slicing only model shows poor performances, while the use of the PW-MLP classifier helps the full backbone architecture to improve the quality of the segmentations. In contrast, on the WHU-CD the architecture with sliced backbone and the PW-MLP classifier obtains better scores than the one with full backbone but without PW-MLP, remaining the performances of the latter still unsatisfactory and far from those obtained by our model.

Table 4: Performance comparison between versions of our model including and excluding the backbone slicing and the PW-MLP classifier.

LEVIR-CD						
Model	Precision	Recall	F1 score	IoU	Accuracy	Params
Full w/o MLP	83.05	94.00	88.19	78.88	98.71	17740598
Full w MLP	92.65	89.26	90.92	83.36	99.09	17743288
Sliced w/o MLP	46.15	94.52	62.02	44.95	94.10	282438
Sliced w MLP	92.68	89.47	91.05	83.57	99.10	285128
WHU-CD						
Model	Precision	Recall	F1 score	IoU	Accuracy	Params
Full w/o MLP	43.08	88.12	57.87	40.72	94.91	17740598
Full w MLP	91.00	92.14	91.57	84.45	99.32	17743288
Sliced w/o MLP	76.16	89.05	82.10	69.64	98.84	282438
Sliced w MLP	91.72	91.76	91.74	84.74	99.34	285128

4.5.2 Impact of skip connection with MAMB

To quantitatively confirm the usefulness of the skip connections, we trained a model without them and compared the achieved results in Table 5.

Table 5: Performance comparison between the model with/without skip connections on both datasets LEVIR-CD and WHU-CD.

LEVIR-CD					
Model type	Pr	Rc	F1	IoU	OA
No Skip	92.35	88.50	90.38	82.45	99.04
Skip	92.68	89.47	91.05	83.57	99.10
WHU-CD					
Model type	Pr	Rc	F1	IoU	OA
No Skip	90.56	89.77	90.16	82.09	99.22
Skip	91.72	91.76	91.74	84.74	99.34

As can be seen, all the metrics confirm the beneficial effects of skip connections in the model. In Figure 4 we reported an example of the intermediate masks that our model creates in the skip-connections.

As can be seen, the masks created with the MAMB block at resolution 64 highlight the objects that must be tracked (red pixels). The intermediate masks at resolution 128 act more like an edge detector. Finally, the masks at resolution 256, obtained applying the MAMB block directly to the original images I_1 and I_2 , distinguish between object classes like buildings and street (dark blue), vegetation (light green), and shadows (red). The ability to highlight shadows is very effective since it helps the model to detect objects and to refine their edges.

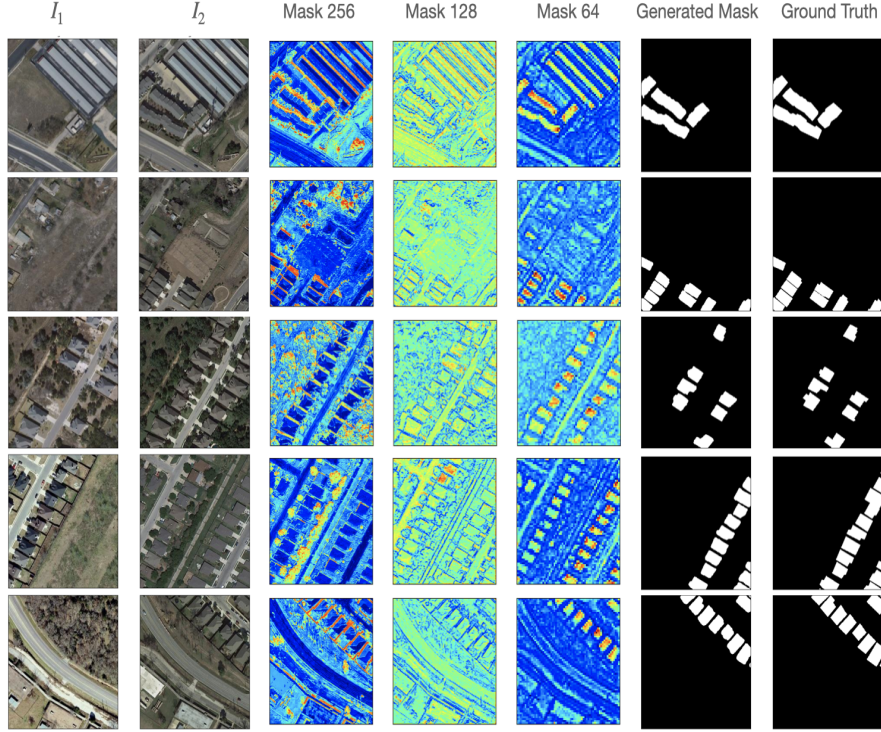


Figure 4: Visualization of the intermediate masks at different resolutions and the final binary mask for one example image pair.

4.5.3 Comparison with other simple mixing strategy

In Table 6 we compare our mixing strategy, described in Section 3.3.1, with other widely used feature fusion blocks. We tested the following alternatives:

- subtraction, both in the bottleneck and in skip connections;
- concatenation + convolution, both in the bottleneck and in skip connections.

We selected these two alternatives since our mixing strategy can be seen as a generalization of the pixel-wise subtraction⁶. However, our mixing block Section 3.3.1 is fully trainable with the spirit of feature re-use [68]. Moreover, concatenation + convolution can be seen as generalization of our mixing block. However, the number of trainable parameters to be tuned for this mixing block is much bigger than ours. More precisely, the number of parameters in our mixing block is $c(2 \cdot k_h \cdot k_w)$,⁷ where c is the number of channels, k_h , k_w are the convolutional kernel sizes. By comparison, a convolution working on the concatenated feature tensors contains $c(2c \cdot k_h \cdot k_w)$ parameters.

In Table 7 we reported the results of a more detailed study on mixing strategies. We alternated the use of subtraction/concatenation + convolution with our respective proposal to mix the features in the bottleneck/skip connections.

The obtained results confirm that our proposal can be considered an effective generalization of the subtraction, with little impact on the size and complexity of the model. On the other hand, the overhead introduced by the concatenation + convolution mixing strategy, seems to produce little differences in terms of performance.

4.5.4 Channel-wise MLP vs CycleMLP

As reported in Section 2.4, several MLP blocks have recently been studied with the intent of incorporating both spatial and channel-specific information. As previously described, we used the MLPs only along the channels in the final classifier, and coupled to our mixing strategy in the MAMB blocks to obtain space-time correlation. We then decided

⁶In fact, if we initialize all of our 2-depth kernels with the "central" weights to 1 and -1 , and all the rest to 0, we have the standard subtraction.

⁷The parentheses are highlighting the size of each kernel and the number of kernels.

Table 6: Performance comparison between the model with our mixing strategy, subtraction, and concatenation + convolution (C+C) respectively.

LEVIR-CD							
Model type	Pr	Rc	F1	IoU	OA	Param. tot.	GFLOPs \pm
Subtraction	92.13	89.41	90.75	83.07	99.07	282939	1.43 (−1.4%)
C+C	92.55	89.61	91.06	83.59	99.10	368468	1.75 (+20.7%)
Our	92.68	89.47	91.05	83.57	99.10	285128	1.45
WHU-CD							
Model type	Pr	Rc	F1	IoU	OA	Param. tot.	GFLOPs \pm
Subtraction	90.10	91.55	90.82	83.19	99.26	282939	1.43 (−1.4%)
C+C	92.19	91.25	91.72	84.71	99.34	368468	1.75 (+20.7%)
Our	91.72	91.76	91.74	84.74	99.34	285128	1.45

Table 7: Evaluation of subtraction and concatenation + convolution mixing strategies. We reported F1 score for the two datasets LEVIR-CD (F1-L) and WHU-CD (F1-W). We used \times to indicate where we changed our proposed option with subtraction or concatenation + convolution. In contrast, \checkmark represents our bottleneck mixing block or MAMB.

(a) Subtraction					(b) Concatenation+Convolution				
Mix	Skip	F1-L	F1-W	Param	Mix	Skip	F1-L	F1-W	Param
\times	\times	90.75	90.82	282939	\times	\times	91.06	91.72	368468
\checkmark	\times	90.75	91.51	284004	\checkmark	\times	91.06	91.08	313028
\times	\checkmark	90.71	89.58	284063	\times	\checkmark	90.90	91.71	340568
\checkmark	\checkmark	91.05	91.74	285128	\checkmark	\checkmark	91.05	91.74	285128

to deal with the CycleMLP block proposed in [45]. The results reported in Table 8 suggest the superiority of our proposed use of MLPs compared to that proposed in [45]. A heuristic explanation for these results can be the following: the MLP blocks proposed in [45] have shown to obtain excellent performances when they are used to construct a hierarchical architecture to generate pyramid features. This makes us think that the advantage of CycleMLPs may be more significant when the features are more refined than the low-level features we use.

5 Limitations of our work

In all the experiments we performed, we observed our model learning some domain-specific patterns. Despite being this an advantage allowing the model to better deal with the faced task, this is also a limitation because it reduces the model’s ability to adapt to new scenarios by means of fine-tuning. Furthermore, in the two datasets taken into consideration, and also in our industrial case study, the images I_1 and I_2 are spatially registered. This allowed the successful usage of low-level features without assessing to global feature relationships. In different contexts, where the images undergo large spatial shifts, this local approach can show worse performances with respect to more global approaches like vision transformers [18, 19].

6 Conclusions and future works

Guided by industrial needs, we proposed a tiny convolutional change-detection Siamese U-Net like model.

Our model exploits low-level features by comparing and classifying them to obtain a binary map of detected changes. We propose a mixing block showing the ability to compare/compose features on both spatial and temporal domains. The proposed PW-MLP block shows great ability in extracting features useful to classify occurred changes on a per-pixel basis. The composition of these proposed blocks, here referred as MAMB, shows the ability to estimate masks useful to

Table 8: Performance comparison between MLP and CycleMLP [45] on LEVIR-CD and WHU-CD. We used ✗ to indicate experiments where we changed our proposed block with a CycleMLP one, while ✓ represents our proposed architecture.

LEVIR-CD							
Skip	Class.	Pr	Rc	F1	IoU	OA	Param. tot.
✗	✓	92.47	88.48	90.43	82.53	99.04	309300
✗	✗	92.45	88.49	90.42	82.52	99.04	314542
✓	✗	92.58	88.96	90.73	83.04	99.07	290370
✓	✓	92.68	89.47	91.05	83.57	99.10	285128
WHU-CD							
Skip	Class.	Pr	Rc	F1	IoU	OA	Param. tot.
✗	✓	89.76	89.06	89.41	80.85	99.16	309300
✗	✗	92.25	90.51	91.37	84.12	99.32	314542
✓	✗	90.20	85.84	87.96	78.52	99.06	290370
✓	✓	91.72	91.76	91.74	84.74	99.34	285128

enrich features used in the U-Net decoder part. We have shown that an effective way to generate the output mask is to process low-level backbone features in a PW-MLP block, effectively facing the change-detection task as a per-pixel classification problem.

We tested our model on public change-detection datasets containing aerial images acquired at two different times. Furthermore, we compared the achieved results with SOTA models proposed in the change-detection literature. Our tests demonstrated that our model performs comparably or better than the current SOTA models, remaining at the same time the smaller and faster one.

Notice that the ideas employed in this work can be also applied to other fields. For this reason, we will investigate the application of MAMB and PW-MLP blocks to tasks such as anomaly-detection, surveillance, and semantic segmentation.

As a future work, solutions to the limitations presented in 5 will be investigated. Moreover, in order to be able to extend our approach even in those contexts where global features play a fundamental role, we would like to explore multibranch models in which one branch works on local features and one on global features.

Acknowledgments

The authors want to thank the whole ARGO Vision team, professor Stefano Gualandi, Gabriele Loli and Gennaro Auricchio for the useful discussion and comments. We also want to thank all those who have provided their codes in an accessible and reproducible way. The Ph.D. scholarship of Andrea Codegoni is founded by SeaVision s.r.l..

A Backbones comparison

In this appendix we report the results obtained by varying the backbone adopted in the model. In each backbone we select only few initial blocks in order to work with features that are not very complex and not excessively aggregated from a spatial point of view. We decide to select the all the initial blocks up to the first having spatial resolution 32×32 . Due to the different compositions of the considered networks, the final size of the models changes in the range starting from a minimum of 32k parameters up to 1.3M.

As we can see from Table 9, the results obtained are stable from the performances point of view. The backbones of the EfficientNet family appear to be, in accordance with the experiments carried out on our proprietary dataset, those that achieve the best performances. However, the other backbone types also produce comparable results making our approach:

- robust with respect to the backbone used;
- flexible with respect to the required size and computational complexity.

In this comparison we have not considered Transformers-type backbones such as [69, 70]. The reason for this choice lies in the fact that the philosophy of the Transformers is a global philosophy, as opposed to the blocks we propose which are instead local. As mentioned in Section 6, an integration of these two philosophies will be the subject of future works.

Table 9: Comparison of different backbones on LEVIR-CD dataset

LEVIR-CD						
Backbone	Precision	Recall	F1 score	IoU	Accuracy	Params
mobilenetv2	90.95	86.43	88.63	79.59	98.87	38798
mobilenetv3large	90.56	85.98	88.21	78.91	98.82	32886
resnet18	92.15	87.43	89.72	81.37	98.98	707894
efficientnetb0	92.18	87.96	90.02	81.85	99.00	79480
efficientnetb1	92.17	88.92	90.51	82.67	99.05	122092
efficientnetb2	92.13	89.26	90.68	82.94	99.06	148040
efficientnetb3	92.40	89.54	90.95	83.40	99.09	178716
efficientnetb4	92.68	89.47	91.05	83.57	99.10	285128
mnasnet13	91.95	88.17	90.02	81.86	99.00	97262
densenet121	92.13	87.97	90.00	81.83	99.00	1364790

B Hyperparameters’ tuning

In this appendix we report the details about the hyperparameters’ tuning experiments. One of the advantages of using limited computational complexity models is being able to fine-tune hyperparameters using relatively few computational resources and in a reasonable time from an industrial point of view. In our experiments we tune the learning rate, the weight decay, and the usage of the *amsgrad* strategy. The framework used to run the experiments and optimize the hyperparameters is NNI [65].

Since we execute only 100 epochs per run, we chose a higher learning rate range (10^{-3} , $4 \cdot 10^{-3}$), in order to explore whether a higher than standard learning rate leads to faster model convergence. As for the weight decay, we follow a conservative choice by setting the range between 10^{-2} and $8 \cdot 10^{-3}$. We also test other simple loss functions for model training such as Mean Square Error (MSE), Intersection over Union (IoU) and a combination of IoU and BCE.

In Figure 5 we show the various combinations of hyperparameters explored in a batch of 30 experiments, and the relative performances on the LEVIR-CD validation set. Analyzing the results, we note that BCE and MSE, regardless of the other parameters, obtain superior performance compared to the IoU. In addition, the BCE + IoU combination, although better than IoU, also scores lower than the BCE and MSE. Regarding the other hyperparameters, as can be seen in particular from Figure 6, our model obtains robust performances with respect to all the tested combinations.

Finally, we note that in the conducted experiments, BCE has lower variance in terms of F1 score with respect to the choices of the other hyperparameters. This represents another motivation for us to chose BCE as loss function.

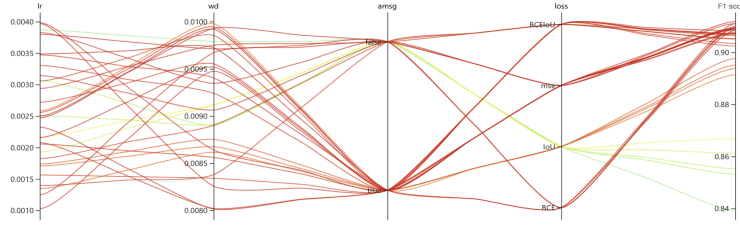


Figure 5: Different combination of parameters and their impact on the F1 score on the LEVIR-CD dataset.

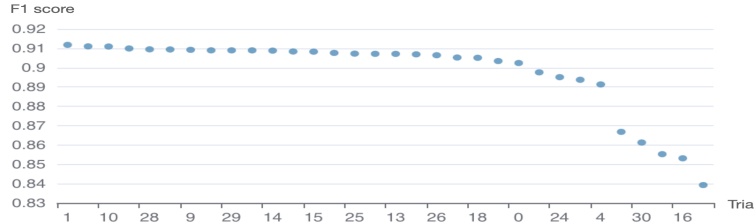


Figure 6: Behavior of the final F1 score in the different experiments conducted to tune the hyperparameters. The drop in the F1 score is due to the use of IoU as loss function.

References

- [1] A. Singh, "Review article digital change detection techniques using remotely-sensed data," *International Journal of Remote Sensing*, vol. 10, no. 6, pp. 989–1003, 1989.
- [2] A. Shafique, G. Cao, Z. Khan, M. Asad, and M. Aslam, "Deep learning-based change detection in remote sensing images: a review," *Remote Sensing*, vol. 14, no. 4, p. 871, 2022.
- [3] T. Bai, L. Wang, D. Yin, K. Sun, Y. Chen, W. Li, and D. Li, "Deep learning for change detection in remote sensing: a review," *Geo-spatial Information Science*, pp. 1–27, 2022.
- [4] H. Chen and Z. Shi, "A spatial-temporal attention-based method and a new dataset for remote sensing image change detection," *Remote Sensing*, vol. 12, no. 10, p. 1662, 2020.
- [5] P. P. De Bem, O. A. de Carvalho Junior, R. Fontes Guimarães, and R. A. Trancoso Gomes, "Change detection of deforestation in the brazilian amazon using landsat data and convolutional neural networks," *Remote Sensing*, vol. 12, no. 6, p. 901, 2020.
- [6] A. Viña, F. R. Echavarria, and D. C. Rundquist, "Satellite change detection analysis of deforestation rates and patterns along the colombia–ecuador border," *AMBIO: A Journal of the Human Environment*, vol. 33, no. 3, pp. 118–125, 2004.
- [7] J. Z. Xu, W. Lu, Z. Li, P. Khaitan, and V. Zaytseva, "Building damage detection in satellite imagery using convolutional neural networks," *arXiv preprint arXiv:1910.06444*, 2019.
- [8] C. Zhang, P. Yue, D. Tapete, L. Jiang, B. Shangguan, L. Huang, and G. Liu, "A deeply supervised image fusion network for change detection in high resolution bi-temporal remote sensing images," *ISPRS Journal of Photogrammetry and Remote Sensing*, vol. 166, pp. 183–200, 2020.
- [9] S. Ji, S. Wei, and M. Lu, "Fully convolutional networks for multisource building extraction from an open aerial and satellite imagery data set," *IEEE Transactions on Geoscience and Remote Sensing*, vol. 57, no. 1, pp. 574–586, 2018.
- [10] A. Varghese, J. Gubbi, A. Ramaswamy, and P. Balamuralidhar, "Changenet: A deep learning architecture for visual change detection," in *European Conference on Computer Vision*, 2018, pp. 129–145.
- [11] L. Khelifi and M. Mignotte, "Deep learning for change detection in remote sensing images: Comprehensive review and meta-analysis," *IEEE Access*, vol. 8, pp. 126 385–126 400, 2020.

- [12] R. C. Daudt, B. Le Saux, and A. Boulch, "Fully convolutional siamese networks for change detection," in *IEEE International Conference on Image Processing*, 2018, pp. 4063–4067.
- [13] M. Zhang, G. Xu, K. Chen, M. Yan, and X. Sun, "Triplet-based semantic relation learning for aerial remote sensing image change detection," *IEEE Geoscience and Remote Sensing Letters*, vol. 16, no. 2, pp. 266–270, 2018.
- [14] Y. Liu, C. Pang, Z. Zhan, X. Zhang, and X. Yang, "Building change detection for remote sensing images using a dual-task constrained deep siamese convolutional network model," *IEEE Geoscience and Remote Sensing Letters*, vol. 18, no. 5, pp. 811–815, 2020.
- [15] D. Peng, Y. Zhang, and H. Guan, "End-to-end change detection for high resolution satellite images using improved unet++," *Remote Sensing*, vol. 11, no. 11, p. 1382, 2019.
- [16] H. Jiang, X. Hu, K. Li, J. Zhang, J. Gong, and M. Zhang, "Pga-siamnet: Pyramid feature-based attention-guided siamese network for remote sensing orthoimagery building change detection," *Remote Sensing*, vol. 12, no. 3, p. 484, 2020.
- [17] J. Chen, Z. Yuan, J. Peng, L. Chen, H. Huang, J. Zhu, Y. Liu, and H. Li, "Dasnet: Dual attentive fully convolutional siamese networks for change detection in high-resolution satellite images," *IEEE Journal of Selected Topics in Applied Earth Observations and Remote Sensing*, vol. 14, pp. 1194–1206, 2020.
- [18] H. Chen, Z. Qi, and Z. Shi, "Remote sensing image change detection with transformers," *IEEE Transactions on Geoscience and Remote Sensing*, pp. 1–14, 2021.
- [19] W. G. C. Bandara and V. M. Patel, "A transformer-based siamese network for change detection," in *IEEE International Geoscience and Remote Sensing Symposium*, 2022, pp. 207–210.
- [20] S. Chen, K. Yang, and R. Stiefelhagen, "Dr-tanet: dynamic receptive temporal attention network for street scene change detection," in *IEEE Intelligent Vehicles Symposium*, 2021, pp. 502–509.
- [21] S. Chopra, R. Hadsell, and Y. LeCun, "Learning a similarity metric discriminatively, with application to face verification," in *Proceedings of the IEEE Conference on Computer Vision and Pattern Recognition*, vol. 1, 2005, pp. 539–546.
- [22] S. Zagoruyko and N. Komodakis, "Learning to compare image patches via convolutional neural networks," in *Proceedings of the IEEE Conference on Computer Vision and Pattern Recognition*, 2015, pp. 4353–4361.
- [23] S. Stent, R. Gherardi, B. Stenger, and R. Cipolla, "Detecting change for multi-view, long-term surface inspection," in *Proceedings of the British Machine Vision Conference*, September 2015, pp. 127.1–127.12.
- [24] J. Long, E. Shelhamer, and T. Darrell, "Fully convolutional networks for semantic segmentation," in *Proceedings of the IEEE conference on Computer Vision and Pattern Recognition*, 2015, pp. 3431–3440.
- [25] O. Ronneberger, P. Fischer, and T. Brox, "U-net: Convolutional networks for biomedical image segmentation," in *International Conference on Medical image computing and computer-assisted intervention*, 2015, pp. 234–241.
- [26] L. Bertinetto, J. Valmadre, J. F. Henriques, A. Vedaldi, and P. H. Torr, "Fully-convolutional siamese networks for object tracking," in *European Conference on Computer Vision*, 2016, pp. 850–865.
- [27] A. Ioannidou, E. Chatzilari, S. Nikolopoulos, and I. Kompatsiaris, "Deep learning advances in computer vision with 3d data: A survey," *ACM Computing Surveys CSUR*, vol. 50, no. 2, pp. 1–38, 2017.
- [28] Y. Chu, G. Cao, and H. Hayat, "Change detection of remote sensing image based on deep neural networks," in *International Conference on Artificial Intelligence and Industrial Engineering*, 2016, pp. 262–267.
- [29] J. Bromley, I. Guyon, Y. LeCun, E. Säckinger, and R. Shah, "Signature verification using a "siamese" time delay neural network," *Advances in Neural Information Processing Systems*, vol. 6, pp. 737–744, 1993.
- [30] M. Lebedev, Y. V. Vizilter, O. Vygolov, V. Knyaz, and A. Y. Rubis, "Change detection in remote sensing images using conditional adversarial networks," *International Archives of the Photogrammetry, Remote Sensing & Spatial Information Sciences*, vol. 42, no. 2, pp. 565–571, 2018.
- [31] W. Zhao, X. Chen, X. Ge, and J. Chen, "Using adversarial network for multiple change detection in bitemporal remote sensing imagery," *IEEE Geoscience and Remote Sensing Letters*, pp. 1–5, 2020.
- [32] X. Peng, R. Zhong, Z. Li, and Q. Li, "Optical remote sensing image change detection based on attention mechanism and image difference," *IEEE Transactions on Geoscience and Remote Sensing*, vol. 59, no. 9, pp. 7296–7307, 2020.
- [33] T. Bao, C. Fu, T. Fang, and H. Huo, "Ppcnet: A combined patch-level and pixel-level end-to-end deep network for high-resolution remote sensing image change detection," *IEEE Geoscience and Remote Sensing Letters*, vol. 17, no. 10, pp. 1797–1801, 2020.

- [34] B. Hou, Q. Liu, H. Wang, and Y. Wang, "From w-net to cdgan: Bitemporal change detection via deep learning techniques," *IEEE Transactions on Geoscience and Remote Sensing*, vol. 58, no. 3, pp. 1790–1802, 2019.
- [35] Y. Zhan, K. Fu, M. Yan, X. Sun, H. Wang, and X. Qiu, "Change detection based on deep siamese convolutional network for optical aerial images," *IEEE Geoscience and Remote Sensing Letters*, vol. 14, no. 10, pp. 1845–1849, 2017.
- [36] B. Fang, L. Pan, and R. Kou, "Dual learning-based siamese framework for change detection using bi-temporal vhr optical remote sensing images," *Remote Sensing*, vol. 11, no. 11, p. 1292, 2019.
- [37] H. Chen, W. Li, and Z. Shi, "Adversarial instance augmentation for building change detection in remote sensing images," *IEEE Transactions on Geoscience and Remote Sensing*, vol. 60, pp. 1–16, 2021.
- [38] K. He, X. Zhang, S. Ren, and J. Sun, "Deep residual learning for image recognition," in *Proceedings of the IEEE Conference on Computer Vision and Pattern Recognition*, 2016, pp. 770–778.
- [39] K. Simonyan and A. Zisserman, "Very deep convolutional networks for large-scale image recognition," in *International Conference on Learning Representations*, 2015, pp. 1–14.
- [40] L.-C. Chen, G. Papandreou, I. Kokkinos, K. Murphy, and A. L. Yuille, "Deeplab: Semantic image segmentation with deep convolutional nets, atrous convolution, and fully connected crfs," *IEEE Transactions on Pattern Analysis and Machine Intelligence*, vol. 40, no. 4, pp. 834–848, 2017.
- [41] X. Wang, R. Girshick, A. Gupta, and K. He, "Non-local neural networks," in *Proceedings of the IEEE conference on Computer Vision and Pattern Recognition*, 2018, pp. 7794–7803.
- [42] T. Liu, L. Yang, and D. Lunga, "Change detection using deep learning approach with object-based image analysis," *Remote Sensing of Environment*, vol. 256, p. 112308, 2021.
- [43] B. Wu, C. Xu, X. Dai, A. Wan, P. Zhang, Z. Yan, M. Tomizuka, J. Gonzalez, K. Keutzer, and P. Vajda, "Visual transformers: Token-based image representation and processing for computer vision," *arXiv preprint arXiv:2006.03677*, 2020.
- [44] A. Vaswani, N. Shazeer, N. Parmar, J. Uszkoreit, L. Jones, A. N. Gomez, Ł. Kaiser, and I. Polosukhin, "Attention is all you need," *Advances in Neural Information Processing Systems*, vol. 30, pp. 6000–6010, 2017.
- [45] S. Chen, E. Xie, G. Chongjian, R. Chen, D. Liang, and P. Luo, "Cyclemlp: A mlp-like architecture for dense prediction," in *International Conference on Learning Representations*, 2022.
- [46] D. Lian, Z. Yu, X. Sun, and S. Gao, "As-mlp: An axial shifted mlp architecture for vision," in *International Conference on Learning Representations*, 2022.
- [47] J. Zhang, K. Yang, C. Ma, S. Reiß, K. Peng, and R. Stiefelhagen, "Bending reality: Distortion-aware transformers for adapting to panoramic semantic segmentation," in *Proceedings of the IEEE/CVF Conference on Computer Vision and Pattern Recognition*, 2022, pp. 16 917–16 927.
- [48] I. O. Tolstikhin, N. Houlsby, A. Kolesnikov, L. Beyer, X. Zhai, T. Unterthiner, J. Yung, A. Steiner, D. Keysers, J. Uszkoreit *et al.*, "Mlp-mixer: An all-mlp architecture for vision," *Advances in Neural Information Processing Systems*, vol. 34, pp. 24 261–24 272, 2021.
- [49] H. Touvron, P. Bojanowski, M. Caron, M. Cord, A. El-Nouby, E. Grave, G. Izacard, A. Joulin, G. Synnaeve, J. Verbeek *et al.*, "Resmlp: Feedforward networks for image classification with data-efficient training," *IEEE Transactions on Pattern Analysis and Machine Intelligence*, 2022.
- [50] H. Liu, Z. Dai, D. So, and Q. V. Le, "Pay attention to mlps," *Advances in Neural Information Processing Systems*, vol. 34, pp. 9204–9215, 2021.
- [51] T. Yu, X. Li, Y. Cai, M. Sun, and P. Li, "S2-mlp: Spatial-shift mlp architecture for vision," in *Proceedings of the IEEE/CVF Winter Conference on Applications of Computer Vision*, 2022, pp. 297–306.
- [52] K. He, X. Zhang, S. Ren, and J. Sun, "Delving deep into rectifiers: Surpassing human-level performance on imagenet classification," in *Proceedings of the IEEE/CVF International Conference on Computer Vision*, 2015, pp. 1026–1034.
- [53] D. Ulyanov, A. Vedaldi, and V. Lempitsky, "Instance normalization: The missing ingredient for fast stylization," *arXiv preprint arXiv:1607.08022*, 2016.
- [54] S. Hochreiter, Y. Bengio, P. Frasconi, and J. Schmidhuber, "Gradient flow in recurrent nets: the difficulty of learning long-term dependencies," *A field guide to dynamical recurrent neural networks.*, pp. 237–244, 2001.
- [55] S. Hochreiter and J. Schmidhuber, "Long short-term memory," *Neural computation*, vol. 9, no. 8, pp. 1735–1780, 1997.

- [56] M. Tan and Q. Le, “Efficientnet: Rethinking model scaling for convolutional neural networks,” in *International Conference on Machine Learning*, 2019, pp. 6105–6114.
- [57] J. Deng, W. Dong, R. Socher, L.-J. Li, K. Li, and L. Fei-Fei, “Imagenet: A large-scale hierarchical image database,” in *Proceedings of the IEEE Conference on Computer Vision and Pattern Recognition*, 2009, pp. 248–255.
- [58] N. Liu, J. Han, and M.-H. Yang, “Picanet: Learning pixel-wise contextual attention for saliency detection,” in *Proceedings of the IEEE Conference on Computer Vision and Pattern Recognition*, 2018, pp. 3089–3098.
- [59] M. Lin, Q. Chen, and S. Yan, “Network in network,” in *International Conference on Learning Representations*, 2014.
- [60] L. Sifre and S. Mallat, “Rigid-motion scattering for texture classification,” *Computer Science*, vol. 3559, pp. 501–515, 2014.
- [61] F. Chollet, “Xception: Deep learning with depthwise separable convolutions,” in *Proceedings of the IEEE Conference on Computer Vision and Pattern Recognition*, 2017, pp. 1251–1258.
- [62] W. G. C. Bandara and V. M. Patel, “Revisiting consistency regularization for semi-supervised change detection in remote sensing images,” *arXiv preprint arXiv:2204.08454*, 2022.
- [63] A. Paszke, S. Gross, F. Massa, A. Lerer, J. Bradbury, G. Chanan, T. Killeen, Z. Lin, N. Gimeshein, L. Antiga *et al.*, “Pytorch: An imperative style, high-performance deep learning library,” *Advances in Neural Information Processing Systems*, vol. 32, 2019.
- [64] I. Loshchilov and F. Hutter, “Decoupled weight decay regularization,” *arXiv preprint arXiv:1711.05101*, 2017.
- [65] Microsoft, “Neural Network Intelligence,” 2021. [Online]. Available: <https://github.com/microsoft/nni>
- [66] I. Loshchilov and F. Hutter, “SGDR: Stochastic Gradient Descent with Warm Restarts,” in *International Conference on Learning Representations*, 2019.
- [67] A. Buslaev, V. I. Iglovikov, E. Khvedchenya, A. Parinov, M. Druzhinin, and A. A. Kalinin, “Albumentations: fast and flexible image augmentations,” *Information*, vol. 11, no. 2, p. 125, 2020.
- [68] Y. Bengio, A. Courville, and P. Vincent, “Representation learning: A review and new perspectives,” *IEEE Transactions on Pattern Analysis and Machine Intelligence*, vol. 35, no. 8, pp. 1798–1828, 2013.
- [69] Z. Liu, Y. Lin, Y. Cao, H. Hu, Y. Wei, Z. Zhang, S. Lin, and B. Guo, “Swin transformer: Hierarchical vision transformer using shifted windows,” in *Proceedings of the IEEE/CVF International Conference on Computer Vision*, 2021, pp. 10 012–10 022.
- [70] A. Dosovitskiy, L. Beyer, A. Kolesnikov, D. Weissenborn, X. Zhai, T. Unterthiner, M. Dehghani, M. Minderer, G. Heigold, S. Gelly, J. Uszkoreit, and N. Houlsby, “An image is worth 16x16 words: Transformers for image recognition at scale,” in *International Conference on Learning Representations*, 2020.